mation and against a random distribution of stacking faults in the polytypes is overwhelming.

The observation (see Fig. 1) that the asymptotic value of N_R/N_L is two indicates that the transformation mechanism does contribute to the randomization of layer positions so that for structures created by a large number of transformations the type of the layer in the $M+1$ position does indeed become randomly related to the first one. This however does not imply that the stacking faults are randomly distributed.

References

MARDIX, S. (1986*a*). *Phys. Rev. B*, **33**, 8677-8684.
MARDIX, S. (1986*b*). *Bull. Mineral.* **109**, 131-142.
PAULING, L. (1945). *The Nature of the Chemical Bond.* Ithaca, New York: Cornell Univ. Press.
STEINBERGER, I. T. (1973). *Philos. Mag.* **27**, 159-175.
STEINBERGER, I. T. (1983). *Progress in Crystal Growth and Characterization*, Vol. 7, edited by P. KRISHNA, pp. 7-53. Oxford: Pergamon Press.
ZHDANOV, G. S. (1945). *C. R. (Dokl.) Acad. Sci. URSS*, **48**, 40-43.

Acta Cryst. (1991). A**47**, 180-195

Anisotropy of Anomalous Dispersion in X-ray Diffraction

BY A. KIRFEL AND A. PETCOV

Universität des Saarlandes, FR Kristallographie, WD-6600 Saarbrücken 11, Germany

AND K. EICHHORN

Hamburger Synchrotronstrahlungslabor HASYLAB am Deutschen Elektronen-Synchrotron DESY, Notkestrasse 85, WD-2000 Hamburg 52, Germany

(*Received* 1 *June* 1990; *accepted* 16 *October* 1990)

Abstract

Polarization-dependent resonant Bragg diffraction in crystals is investigated both theoretically and experimentally. In order to describe the effects of anisotropic anomalous dispersion on intensity and polarization of kinematically diffracted X-radiation, a general scattering model is developed on the basis of site-symmetry-compatible second-rank scattering-factor tensors for the absorbing atoms. For conventional four-circle single-crystal diffractometry it is shown that intensity and polarization of the diffracted beam can be predicted as functions of both crystal orientation and polarization of the incident radiation. In principle, anisotropy of anomalous dispersion may affect any reflection. In particular, it can give rise to the observation of intensities for reflections being systematically extinct by space-group symmetry. Both effects are discussed. Experimental proof of the model's validity was obtained by synchrotron-radiation X-ray diffraction measurements of mainly 'forbidden' reflections in cubic cuprite, Cu_2O and tetragonal rutile type TiO_2 and MnF_2. The experiments were carried out at the respective K-absorption edges of the cations using different instruments at HASYLAB/DESY during dedicated mode of DORIS II (3·78 GeV). Significant anisotropy of anomalous dispersion due to excitation of K electrons into p states was observed in each case, allowing studies of the dependence of 'forbidden' reflection intensities on both radiation energy and rotation (Ψ) around the scattering vector **h**. Comparison of the observations with the analytical intensity functions derived from the scattering model shows full agreement on a relative scale. For cuprite, estimates of the anisotropies of the real and imaginary components of the anomalous dispersion of Cu were obtained from the allowed reflection 330. The values derived from two different experiments (energies) are $f' = -0{\cdot}56$, $-0{\cdot}35$ and $f'' = -0{\cdot}23$, $0{\cdot}0$ electrons, respectively.

Introduction

The anisotropy of the anomalous dispersion (AAD) of X-rays is an energy-dependent resonance effect which is likely to occur in the vicinity of an absorption edge of a bonded atom. As a pure consequence of chemical bonding it reflects two phenomena in the XANES and EXAFS regions, respectively:

(i) dipole and (to a much smaller extent) quadrupole transitions from the initial 'core' state to excited states which are vacant, allowed and related to the local symmetry and the chemical environment of the absorbing 'edge' atom,

(ii) interference of the outgoing wave of 'true' photoelectrons, *i.e.* with positive energy, with the wave backscattered from surrounding neighbor atoms.

In crystalline material of lower than cubic symmetry both effects can manifest themselves in an anisotropic refractive index and consequently in

0108-7673/91/030180-16$03.00

angular-dependent X-ray absorption cross sections which can be studied by transmission of linearly polarized photons (polarized radiation is, however, not a prerequisite). With the advent of synchrotron radiation (SR) the investigation of 'polarized', 'angular dependent' or 'anisotropic' X-ray absorption spectra has become an attractive tool which is meanwhile applied to a broad range of problems in chemistry, mineralogy, biology and solid-state and surface science. A number of applications has been compiled recently by Brouder (1990) who gives a theoretical account of the angular dependence of X-ray absorption spectra.

Within the dipole approximation AAD can be described by assigning to both real and imaginary parts of the anomalous-dispersion correction, f' and f'', energy-dependent second-rank tensors which are compatible with the symmetry of the 'edge' atom. Since the macroscopic refractive index is determined by the average over all AAD tensors in the unit cell, *i.e.* the tensor being invariant against the rotational operations of the space group, AAD has no effect on the X-ray optical isotropy of cubic crystals. It causes, however, X-ray pleochroism and birefringence for all other systems as demonstrated, for example, by Templeton & Templeton (1980, 1982, 1985*a*, *b*, 1988). In uniaxial $LiNbO_3$, birefringence has been studied by Petcov, Kirfel & Fischer (1990) using SR and an experimental set-up analogous to the optical polarization microscope. These investigations were performed to obtain information about AAD in the crystallographic context, while the majority of transmission experiments deals merely with the anisotropy of the photoelectric absorption coefficient μ which contains information about the projected density of states and/or near-neighbor geometry of edge atoms.

The effect of AAD on kinematic single-crystal Bragg diffraction was first discussed by Templeton & Templeton (1980). Based on the fact that, regardless of the crystal symmetry, the intensity of each reflection may be modified in case of AAD, they developed a method for the determination of the principal components of the f', f'' tensors from selected diffraction data. As a particular consequence of AAD, the authors stated in 1980 that 'screw-axis and glide-plane rules for absent reflections are no longer rigorous since crystallographically equivalent atoms do not have exactly the same scattering power'. In two theoretical contributions (Dmitrienko, 1983, 1984) and a recent review (Belyakov & Dmitrienko, 1989), a method was discussed for predicting the properties of this new type of structurally 'forbidden' reflections. Extinction rules and explicit intensity formulae were derived for the cubic system. Apart from our own work (see below and Petcov, 1989), the first and (to our knowledge) only experimental verification of the occurrence of space-group-extinct reflections due to AAD has been reported by Templeton & Templeton (1985*a*, 1986, 1987) for the case of cubic $NaBrO_3$. At the Br K-absorption edge they observed reflections $00l$ with $l = 1, 3, 5, 7, 9, 11$. The intensity dependencies on the azimuthal angle Ψ were in agreement with the prediction by Dmitrienko (1984). In addition, the authors were able to show that this information could be used to determine the phases of the corresponding (allowed) second-order reflections with l even.

In the present paper we wish to contribute to the knowledge of Bragg scattering in the presence of AAD. A general treatment of its effect is attempted on the basis of the Jones calculus (Jones, 1941, 1948), which has been found very useful in the description of the near-edge transmission of polarized radiation through $LiNbO_3$. The formulation of the optical model in terms of Jones vectors and matrices renders a concise notation of both the intensity and polarization of the scattered radiation.

The model is compared to experimental results obtained with SR on single crystals of cubic cuprite, Cu_2O (Kirfel, Petcov, Fischer & Eichhorn, 1988; Eichhorn & Kirfel, 1988; Kirfel & Eichhorn, 1988, 1989) and tetragonal rutile-type TiO_2 (Kirfel & Petcov, 1989) and MnF_2 (Kirfel, Petcov, Jauch & Palmer, 1989) using different instruments at HASYLAB/DESY. The energy-dependent occurrence of space-group-extinct reflections was abbreviated to FRED (*f*orbidden *r*eflection near *e*dge *d*iffraction) and emphasis was put on proving FRED and on the investigation of the intensity variation upon rotation around the scattering vector (Ψ rotation). In case of Cu_2O some allowed reflections were also considered.

The choice of the substances was governed not only by the availability of large single crystals, but also by the fact that the crystal structures are very different. While Cu in cuprite possesses an extremely anisotropic chemical environment provided by a linear O–Cu–O arrangement, the cation in the rutile structure is at center of an almost regular octahedron of O atoms, and only the second-neighbor environment exhibits a distinct anisotropy. Thus, one important aspect in choosing rutile was to elucidate whether or not AAD can be expected in the majority of mineral structures being composed of rather less- than more-distorted coordination polyhedra.

Elastic scattering in the Jones's formalism

The observation of elastic photon scattering under $2\Theta \neq 0$ defines the scattering plane containing both incident and diffracted beams. A totally polarized electromagnetic plane wave can then be represented by the column vector of the electric field:

$$|D\rangle_0 = \begin{pmatrix} A_{0\sigma} \\ A_{0\pi} \end{pmatrix}. \qquad (1)$$

$A_{0\sigma,\pi}$ are generally complex numbers and σ and π denote the components perpendicular and parallel to the scattering plane which may be vertical as depicted in Fig. 1. (D is used for the electric field because in the following E denotes the energy of the radiation.)

$|D\rangle_0$ gives a complete description of the radiation properties. In particular, the intensity is

$$I_0 = {}_0\langle D^*|D\rangle_0 = |A_{0\sigma}|^2 + |A_{0\pi}|^2 \tag{2}$$

and the degree of linear polarization, for example, perpendicular to the scattering plane is

$$P_\sigma = |A_{0\sigma}|^2 / I_0. \tag{3}$$

The effect of a scatterer on $|D\rangle_0$ can be described by a complex scattering operator $\mathcal{F}_\Theta$ so that the scattered radiation is

$$|D\rangle_\Theta = \begin{pmatrix} A_\sigma \\ A_\pi \end{pmatrix} = \mathcal{F}_\Theta |D\rangle_0 \tag{4}$$

and the intensity

$$I_\Theta = {}_\Theta\langle D^*|D\rangle_\Theta = {}_0\langle D^*|\mathcal{F}_\Theta^+ \mathcal{F}_\Theta|D\rangle_0. \tag{5}$$

(The superscripts * and $^+$ denote complex and Hermitian conjugation, respectively.) The individual intensity contributions of the σ- and π-polarized components can be obtained by applying the projection operators:

$$P_\sigma = \begin{pmatrix} 1 & 0 \\ 0 & 0 \end{pmatrix} \quad \text{and} \quad P_\pi = \begin{pmatrix} 0 & 0 \\ 0 & 1 \end{pmatrix},$$

respectively.

With $P^+P = P$ for both cases, one obtains

$$\begin{aligned} I_{\Theta\sigma} &= {}_0\langle D^*|\mathcal{F}_\Theta^+ P_\sigma \mathcal{F}_\Theta|D\rangle_0 \\ I_{\Theta\pi} &= {}_0\langle D^*|\mathcal{F}_\Theta^+ P_\pi \mathcal{F}_\Theta|D\rangle_0, \end{aligned} \tag{6}$$

which, of course, sum up to I_Θ of (5). Consequently, the degree of σ polarization of the diffracted radiation follows from

$$\begin{aligned} P_{\Theta\sigma} &= I_{\Theta\sigma}/(I_{\Theta\sigma} + I_{\Theta\pi}) \\ &= {}_0\langle D^*|\mathcal{F}_\Theta^+ P_\sigma \mathcal{F}_\Theta|D\rangle_0 / {}_0\langle D^*|\mathcal{F}_\Theta^+ \mathcal{F}_\Theta|D\rangle_0. \end{aligned} \tag{6a}$$

Considering the scattering object as an optical element, one can use the formalism introduced by Jones (1941) to describe the scattering operator $\mathcal{F}_\Theta$ by a 2×2 matrix:

$$\mathcal{F}_\Theta = \begin{pmatrix} \Phi_{\sigma'\sigma} & \Phi_{\sigma'\pi} \\ \Phi_{\pi'\sigma} & \Phi_{\pi'\pi} \end{pmatrix} \tag{7}$$

where the elements $\Phi_{\nu'\eta}(\eta, \nu = \sigma, \pi)$ contain a description of the scattering object and determine the properties of the scattered radiation, $|D\rangle_0$. The $\Phi_{\nu'\eta}$ are defined as

$$\Phi_{\nu'\eta} = \mathbf{e}_\nu'^T \mathbf{F}(\mathbf{s}) \mathbf{e}_\eta. \tag{8}$$

$\mathbf{e}_\sigma = \mathbf{e}_\sigma'$, $\mathbf{e}_\pi$ and $\mathbf{e}_\pi'$ are the unit vectors of the polarization directions (T = transpose) with respect to a coordinate system associated with the scattering object, *i.e.* the scattering density distribution which may be a scalar function $\rho(\mathbf{r})$ or a tensor function $\boldsymbol{\rho}(\mathbf{r})$. The same applies to the Fourier transform $F(\mathbf{s})$ or $\mathbf{F}(\mathbf{s})$ ($|\mathbf{s}| = \sin\Theta/\lambda$).

Substitution of (1) and (7) into (5) and (6*a*) yields

$$\begin{aligned} I_\Theta = {} & |A_{0\sigma}|^2(|\Phi_{\sigma'\sigma}|^2 + |\Phi_{\pi'\sigma}|^2) + |A_{0\pi}|^2(|\Phi_{\pi'\pi}|^2 + |\Phi_{\sigma'\pi}|^2) \\ & + 2\,\mathrm{Re}[A_{0\sigma}^* A_{0\pi}(\Phi_{\sigma'\sigma}^* \Phi_{\sigma'\pi} + \Phi_{\pi'\sigma}^* \Phi_{\pi'\pi})] \end{aligned} \tag{9}$$

and

$$\begin{aligned} P_{\Theta\sigma} = {} & (1/I_\Theta)[|A_{0\sigma}|^2 |\Phi_{\sigma'\sigma}|^2 + |A_{0\pi}|^2 |\Phi_{\sigma'\pi}|^2 \\ & + 2\,\mathrm{Re}(A_{0\sigma}^* A_{0\pi} \Phi_{\sigma'\sigma}^* \Phi_{\sigma'\pi})], \end{aligned} \tag{10}$$

which give explicit accounts of the scattered radiation in terms of intensity and degree of σ polarization both as functions of the incident-radiation properties.

Though (9) lacks any assumption about the very nature of the scattering object and is therefore valid for all sorts of samples, it may be exploited to its full extent only if F is not a scalar. This is in particular true for a crystal with atoms exhibiting AAD. The evaluation of $|D\rangle_\Theta$ and I_Θ requires two steps, namely, according to (8):

(i) formulation of the structure factor $\mathbf{F}(\mathbf{h})$; and subsequently

(ii) formulation of the elements $\Phi_{\nu'\eta}(\mathbf{h}, \Psi)$ as functions of the crystal orientation in the laboratory system. Since the polarization directions σ and π have to be considered with respect to the crystal axes, each $\Phi_{\nu'\eta}$ depends also on the azimuthal angle, *i.e.* a Ψ rotation around the scattering vector $\mathbf{h}$.

Once the $\Phi_{\nu'\eta}$ are given, calculations of (4), (9) and (10) are straightforward.

Bragg scattering formalism

In order to describe the AAD of an atom within the dipole approximation the scattering factor is given by an energy-dependent second-rank tensor, $\mathbf{f}$, whose symmetry properties are determined by the point symmetry of the atomic position. This is a natural assumption which, as pointed out by Dmitrienko (1984), has still to be proved both theoretically and experimentally. For any crystal system:

$$\mathbf{f}(E, s) = f_0(s)\mathbf{G}_0^* + \mathbf{f}'(E) + i\mathbf{f}''(E) \tag{11}$$

$$\begin{aligned} \mathbf{f}(E, s) = {} & [f_0(s) + f_0'(E) + if_0''(E)]\mathbf{G}_0^* \\ & + [\mathbf{f}'(E) - f_0'(E)\mathbf{G}_0^*] \\ & + i[\mathbf{f}''(E) - \mathbf{f}_0''(E)\mathbf{G}_0^*], \end{aligned} \tag{11a}$$

where $f_0(s)$ is the non-resonant isotropic atomic scattering factor. $f_0'(E)$, $f_0''(E)$ denote the isotropic components of the anomalous-dispersion correction. $E = h\omega/2\pi$ is the photon energy, $s = (\sin\Theta)/\lambda$ and $\mathbf{G}_0^*$ is the dimensionless tensor obtained from the reciprocal metric tensor for $a^* = b^* = c^* = 1$ (for

orthogonal crystal axes, $\mathbf{G}_0^* = \mathbf{I}$, the unity matrix). Corresponding elements of $\mathbf{f}'$ and $\mathbf{f}''$ are assumed (Templeton & Templeton, 1988) to obey the dispersion relation (James, 1982):

$$f'_{\eta\nu}(\omega) = (2/\pi) \int_0^\infty [\omega' f''_{\eta\nu}(\omega')/(\omega^2 - \omega'^2)]\, \mathrm{d}\omega'. \quad (12)$$

As a consequence of (11), the structure factor of a reflection $\mathbf{h}$ will also be an energy-dependent tensor:

$$\mathbf{F}(\mathbf{h}, E) = \sum_j^n \sum_k^m c_j \mathbf{f}_{jk} T_{jk} G_{jk}. \quad (13)$$

n = number of atoms in the asymmetric unit, m = number of symmetry operations of the space group, c_j = occupation factor, $T_{jk} = \exp[-\mathbf{h}^T \mathbf{B}_{jk} \mathbf{h}]$ = temperature-factor expression, $G_{jk} = \exp[2\pi i \mathbf{h}.\mathbf{r}_{jk}]$ = geometric factor, $\mathbf{f}_{jk}$ is the scattering-factor tensor of the jth atom transformed by the rotational part of the kth symmetry operation (Dmitrienko, 1983) according to

$$\mathbf{f}_{jk} = \mathbf{R}_k \mathbf{f}_{j1} \mathbf{R}_k^T. \quad (14)$$

Thus, the scattering factor $\mathbf{f}_j$ transforms like the tensor of thermal vibration, $\mathbf{B}_j$, yielding in general different scattering amplitudes for crystallographically equivalent atoms. For Bragg diffraction, the interferences due to G_{jk} have to be considered. For $\mathbf{h} = 0$, *i.e.* for X-ray transmission, the superposition $\sum\sum c_j \mathbf{f}_{jk}$ characterizes the macroscopic X-ray optical properties of the crystal.

According to (11a), (13) can be reformulated as

$$\begin{aligned}\mathbf{F}(\mathbf{h}) &= \mathbf{G}_0^* \left[\sum_j^n \sum_k^m c_j (f_{0j} + f'_{0j} + i f''_{0j}) T_{jk} G_{jk} \right] \\ &\quad + \sum_j^n \sum_k^m c_j [(\mathbf{f}'_{jk} - \mathbf{G}_0^* f'_{0j}) + i(\mathbf{f}''_{jk} - \mathbf{G}_0^* f''_{0j})] T_{jk} G_{jk} \\ &= \mathbf{G}_0^* F(\mathbf{h})_0 + \mathbf{F}(\mathbf{h})_a. \quad (15)\end{aligned}$$

The first tensor represents the usual structure factor, $F(\mathbf{h})_0$ (including isotropic anomalous dispersion), whereas the second tensor, $\mathbf{F}(\mathbf{h})_a$, describes solely the contribution due to AAD. Thus, with respect to a Cartesian system (C) attached to the crystal, one can also write:

$$\mathbf{F}(\mathbf{h})_C = \mathbf{I} F(\mathbf{h})_0 + \mathbf{F}(\mathbf{h})_{Ca}. \quad (15a)$$

Substitution of (15a) into (8) transforms (9) into

$$\begin{aligned}I(\mathbf{h}) &= |A_{0\sigma}|^2 [|F_0 + \Phi_{a\sigma'\sigma}|^2 + |\Phi_{a\pi'\sigma}|^2] \\ &\quad + |A_{0\pi}|^2 [|F_0 \cos 2\Theta + \Phi_{a\pi'\pi}|^2 + |\Phi_{a\sigma'\pi}|^2] \\ &\quad + 2\,\mathrm{Re}\{A_{0\sigma}^* A_{0\pi} [\Phi_{a\sigma'\pi}(F_0 + \Phi_{a\sigma'\sigma})^* \\ &\quad + \Phi_{a\pi'\sigma}^* (F_0 \cos 2\Theta + \Phi_{a\pi'\pi})]\}. \quad (16)\end{aligned}$$

This equation shows explicitly that *all* reflection intensities may be affected as soon as the anomalous dispersion of one or more atoms in the asymmetric unit deviates from isotropy. The relative effect may become considerable, especially for weak reflections with systematically or accidentally small $F_0(\mathbf{h})$. Even for $F_0(\mathbf{h}) = 0$, *i.e.* for a reflection which is systematically extinct by space-group symmetry, (16) equals (9) showing the possibility of a non-vanishing intensity. Thus, serial and zonal extinction rules can be violated in the presence of AAD, with an intensity contribution exclusively from the atoms exhibiting the anisotropic resonant scattering.

If (16) is rewritten as

$$I(\mathbf{h}) = I(\mathbf{h})_\sigma + I(\mathbf{h})_\pi + I(\mathbf{h})_{\sigma\pi}, \quad (17)$$

this emphasizes that the first two terms contain the contributions of the orthogonal σ and π components, respectively, regardless of their mutual phase relation, while the third term considers the phase relation between them, *i.e.* the kind of polarization. Clearly, $I(\mathbf{h})_{\sigma\pi}$ vanishes if the radiation is totally σ or π polarized ($|A_{0\sigma}|$ or $|A_{0\pi}| = 0$) or unpolarized. The latter case, however, precludes neither modifications of allowed reflection intensities nor the violation of extinction rules so that polarized radiation is not a prerequisite for the manifestation of AAD in X-ray diffraction. In particular, for $F(\mathbf{h})_0 = 0$ and unpolarized radiation ($|A_{0\sigma}| = |A_{0\pi}| = A_0/2^{1/2}$), one obtains

$$I(\mathbf{h})_u = \tfrac{1}{2} A_0^2 (|\Phi_{a\sigma'\sigma}|^2 + |\Phi_{a\pi'\sigma}|^2 + |\Phi_{a\sigma'\pi}|^2 + |\Phi_{a\pi'\pi}|^2). \quad (18)$$

Vice versa, however, the occurrence of AAD is a necessary condition for a detailed manifestation of the polarization because $I(\mathbf{h})_{\sigma\pi}$ vanishes for $\mathbf{F}(\mathbf{h})_a = 0$ and (16) reduces to the classical

$$I(\mathbf{h}) = |F(\mathbf{h})_0|^2 (|A_{0\sigma}|^2 + |A_{0\pi}|^2 \cos^2 2\Theta) \quad (19)$$

which includes the polarization correction for Thomson scattering, but is ambiguous with respect to the polarization of the radiation. If, for example, $|A_{0\sigma}| = |A_{0\pi}|$, the incident radiation could be linearly or circularly (right or left) polarized or unpolarized.

Scattering intensity of 'forbidden' reflections

Considering in particular 'forbidden' reflections which are systematically extinct due to screw axes and/or glide planes, a detailed discussion of their properties has been given by Dmitrienko (1983). Results were derived on the basis of a suceptibility distribution in the unit cell which is invariant under the symmetry operations. The use of individual $\mathbf{f}$ tensors compatible with the point symmetry of the atoms is more restrictive (Dmitrienko, 1984) because the anisotropy of susceptibility is assumed to be localized at the atomic positions. This leads in some cases to modified structure-factor tensors which may be discussed in more detail elsewhere. Here, we address only a few points concerning some general properties

of 'forbidden' reflections as deduced from the scattering model.

For linear polarization of the incident beam, $I(\mathbf{h})_{\sigma\pi}$ of (17) is given by

$$I(\mathbf{h})_{\sigma\pi} = 2A_{0\sigma}A_{0\pi}\,\mathrm{Re}\,[\Phi_{a\sigma'\pi}\Phi^*_{a\sigma'\sigma} + \Phi^*_{a\pi'\sigma}\Phi_{a\pi'\pi}]. \tag{20}$$

Apart from pure σ or π polarization, $I(\mathbf{h})_{\sigma\pi}$ can only vanish if the bracketed sum equals zero [*e.g.* $\Phi_{a\sigma'\sigma} = \Phi_{a\pi'\pi} = 0$, type I reflections (Dmitrienko, 1983)] or is purely imaginary. In view of (12) the latter cannot be true in general so that the total diffracted intensity is sensitive to (20) if the polarization direction is neither parallel nor perpendicular to the scattering plane.

On the other hand, considering elliptical (circular) polarization with one main axis parallel to the scattering plane:

$$|D\rangle_0 = \begin{pmatrix} A_{0\sigma} \\ \pm iA_{0\pi} \end{pmatrix}$$

$$I(\mathbf{h})_{\sigma\pi} = \mp 2A_{0\sigma}A_{0\pi}\,\mathrm{Im}\,[\Phi_{a\sigma'\pi}\Phi^*_{a\sigma'\sigma} + \Phi^*_{a\pi'\sigma}\Phi_{a\pi'\pi}], \tag{21}$$

which vanishes only if $\mathrm{Im}\,[\mathbf{F}(\mathbf{h})_a] = C\,\mathrm{Re}\,[\mathbf{F}(\mathbf{h})_a]$, C = constant. This condition is met for scattering-factor tensors possessing only one unique off-diagonal element as discussed below. In the general case, however, (21) indicates that the diffracted intensity is different for elliptical (circular) polarizations of opposite sense.

Though the polarization of the diffracted beam is usually not investigated in the diffraction experiment, it is interesting to consider some consequences of the scattering model. The σ polarization of the diffracted radiation is given by (10) which includes both the always present change of polarization due to Bragg diffraction and the change due to an anisotropy of the X-ray susceptibility. These are two different physical phenomena. While the former depends strongly on the crystal perfection, the latter reflects the chemical bonding and the environment of the absorbing atom. Again, for pure σ or π polarization of the incident wave:

$$P(\mathbf{h})_{\sigma\sigma} = |A_{0\sigma}|^2|\Phi_{a\sigma'\sigma}|^2/I(\mathbf{h})_\sigma \tag{22}$$

$$P(\mathbf{h})_{\sigma\pi} = |A_{0\pi}|^2|\Phi_{a\sigma'\pi}|^2/I(\mathbf{h})_\pi. \tag{23}$$

Thus, if $\Phi_{a\sigma'\sigma}$ or $\Phi_{a\pi'\pi} = 0$, the polarization of the diffracted beam is orthogonal to that of the incident one. For these reflections, nonpolarized radiation obviously yields nonpolarized diffracted radiation.

Equation (10) is useful considering linearly or non-polarized radiation, but it fails to give sufficient information about the effect in case of elliptical polarization. Then, one has to refer to (4). As an example, one may consider the special case of circular polarization and again $\Phi_{a\sigma'\sigma} = \Phi_{a\pi'\pi} = 0$:

$$|D\rangle_{\mathbf{h}} = \mathcal{F}A_0\begin{pmatrix} 1 \\ \pm i \end{pmatrix} = A_0\begin{pmatrix} \pm i\Phi_{a\sigma'\pi} \\ \Phi_{a\pi'\sigma} \end{pmatrix}, \tag{24}$$

showing that left-hand circularly polarized radiation is diffracted with right-hand polarization, and *vice versa*, if $\mathbf{F}(\mathbf{h})_a$ is symmetric and $\Phi_{a\sigma'\pi}$ and $\Phi_{a\pi'\sigma}$ are equal and real or imaginary quantities. The same applies to an antisymmetric $\mathbf{F}(\mathbf{h})_a$ and real or imaginary $\Phi_{a\sigma'\pi} = -\Phi_{a\pi'\sigma}$.

The structure factor in the diffractometer system

The formulation of the unit vectors of the polarization directions, $\mathbf{e}_\sigma$, $\mathbf{e}_\pi$ and $\mathbf{e}'_\pi$, with respect to the crystal is equivalent to the description of the structure-factor tensor $\mathbf{F}(\mathbf{h})$ with respect to the diffractometer system (D) after rotation of the crystal into the reflecting position. The notation is analogous to that of Busing & Levy (1967), however, with the usual convention that $\omega = \Theta$ for the bisecting position, *i.e.* the offset $\varepsilon = \omega - \Theta = 0$.

The diffractometer coordinate system (D) for a reflection position is depicted in Fig. 1. The axes X_D and Y_D are in the scattering plane with X_D coinciding with the scattering vector $\mathbf{h}$, and Y_D bisecting the scattering angle 2Θ between the incident and reflected beam.

The orientation of an arbitrarily mounted crystal with respect to the laboratory system is given by the orientation matrix **UB** which contains the components of the reciprocal crystal axes with respect to that system. In order to bring a vector $\mathbf{v}_C$ in the crystal into coincidence with X_D, the crystal has to be rotated around the φ, χ and ω axes of the diffractometer, where the corresponding setting angles are derived from **UB**. Thus,

$$\mathbf{v}_D = \mathbf{EX\Phi v}_L = \mathbf{Qv}_C, \tag{25}$$

where E is the unity matrix for bisecting geometry ($\omega = \varepsilon + \Theta$; $\varepsilon = 0$; **E**, **X** and **Φ** have to be defined

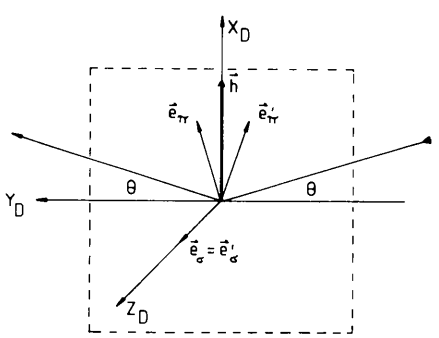

Fig. 1. Scattering geometry for the diffractometer system (D) in the reflection position. The vertical scattering plane contains $\mathbf{e}_\pi$ and $\mathbf{e}'_\pi$.

according to the individual diffractometer set-up and sense of angle rotations). Thus, when a reciprocal-lattice vector $\mathbf{h}$ coincides with X_D, $\mathbf{F(h)}$ has been rotated too. Before applying the rotations $\mathbf{Q}$ to $\mathbf{F(h)}$, one has, however, to consider that $\mathbf{F(h)}$ of (15) is still defined with respect to the reciprocal crystal system which may be oblique. $\mathbf{F(h)}$ must therefore be transformed into a Cartesian system (C) where $X_C \| \mathbf{a}_0$, $Y_C \| \mathbf{c}_0^* \times \mathbf{a}_0$, and $Z_C \| \mathbf{a}_0 \times \mathbf{b}_0$. This is achieved by

$$\mathbf{F(h)}_C = (\mathbf{B}_0^{-1})^T[\mathbf{G}_0^* F(\mathbf{h})_0 + \mathbf{F(h)}_a](\mathbf{B}_0^{-1})$$
$$= \mathbf{I}F(\mathbf{h})_0 + (\mathbf{B}_0^{-1})^T \mathbf{F(h)}_a(\mathbf{B}_0^{-1}) \qquad (26a)$$

with $(\mathbf{B}_0^{-1})^T \mathbf{G}_0^* (\mathbf{B}_0^{-1}) = \mathbf{I}$ and

$$\mathbf{B}_0 = \begin{pmatrix} 1 & \cos\gamma^* & \cos\beta^* \\ 0 & \sin\gamma^* & -\sin\beta^* \cos\alpha \\ 0 & 0 & V_0^*/\sin\gamma^* \end{pmatrix},$$

$$V_0^* = [1 - \cos^2\alpha^* - \cos^2\beta^* - \cos^2\gamma^* + 2\cos\alpha^* \cos\beta^* \cos\gamma^*]^{1/2}.$$

$\mathbf{B}_0$ describes the unit vectors of the reciprocal lattice with respect to system (C), and is the matrix of unity for orthogonal crystal axes. ($\mathbf{B}_0$ can be obtained from the $\mathbf{B}$ matrix by setting $a^* = b^* = c^* = 1$.)

With respect to system (D) one obtains:

$$\mathbf{F(h)}_D = \mathbf{Q}\mathbf{F(h)}_C\mathbf{Q}^T. \qquad (26b)$$

An additional rotation of the crystal around the scattering vector yields

$$\mathbf{F(h;}\ \Psi)_D = \mathbf{\Psi}\mathbf{Q}\mathbf{F(h)}_C\mathbf{Q}^T\mathbf{\Psi}^T \qquad (27)$$

with

$$\mathbf{\Psi} = \begin{pmatrix} 1 & 0 & 0 \\ 0 & \cos\Psi & \sin\Psi \\ 0 & -\sin\Psi & \cos\Psi \end{pmatrix},$$

$\Psi = 0$ refers to the bisecting position ($\omega = \Theta$).

Application of (27) to (8) leads to the final form of the elements $\Phi_{\nu'\eta}$:

$$\Phi_{\nu'\eta}(\mathbf{h};\ \Psi) = \mathbf{e}'^T_{\nu D}\mathbf{\Psi}\mathbf{Q}\mathbf{F(h)}_C\mathbf{Q}^T\mathbf{\Psi}^T\mathbf{e}_{\eta D}. \qquad (28)$$

From Fig. 1 follows:

$$\mathbf{e}_{\sigma D} = \begin{pmatrix} 0 \\ 0 \\ 1 \end{pmatrix}, \quad \mathbf{e}_{\pi D} = \begin{pmatrix} \cos\Theta \\ \sin\Theta \\ 0 \end{pmatrix}, \quad \mathbf{e}'_{\pi D} = \begin{pmatrix} \cos\Theta \\ -\sin\Theta \\ 0 \end{pmatrix}. \qquad (29)$$

Of course, a scalar structure factor $\mathbf{F(h)}_0$ alone yields again:

$$\Phi_{\sigma'\sigma} = F(\mathbf{h})_0, \quad \Phi_{\pi'\pi} = F(\mathbf{h})_0 \cos 2\Theta,$$
$$\Phi_{\pi'\sigma} = \Phi_{\sigma'\pi} = 0.$$

In order to predict the Ψ dependence of the $\Phi_{\nu\eta}$ and ensuingly $I(\mathbf{h};\ \Psi)$, the actual $\mathbf{U}$ is irrelevant and may be taken as the unity matrix, for simplicity. For bisecting geometry ($\varepsilon = 0$), $\mathbf{Q}$ reduces to $\mathbf{Q}_0 = \mathbf{X}_0\mathbf{\Phi}_0$ for which the setting angles χ and φ can be calculated from

$$\varphi = \tan^{-1}(Q_{0,12}/Q_{0,11})$$
$$\chi = \tan^{-1}[Q_{0,13}/(Q_{0,11}^2 + Q_{0,12}^2)^{1/2}] \qquad (30)$$

with

$$Q_{0,1j} = |\mathbf{h}|\mathbf{B}\mathbf{h} \quad [j = 1, 2, 3;\ \mathbf{h} = (h, k, l)]. \qquad (31)$$

Then, with $\Psi = 0$ as defined above, and provided the ambiguities in (30) are properly resolved, (28) can be evaluated explicitly according to:

$$\Phi_{\nu'\eta}(\mathbf{h};\ \Psi) = \mathbf{e}'^T_{\nu D}(\mathbf{\Psi}\mathbf{X}_0\mathbf{\Phi}_0)(\mathbf{B}_0^{-1})^T \times [\mathbf{G}_0^* F(\mathbf{h})_0 + \mathbf{F(h)}_a] \times (\mathbf{B}_0^{-1})(\mathbf{\Psi}\mathbf{X}_0\mathbf{\Phi}_0)^T\mathbf{e}_{\eta D}. \qquad (32)$$

Table 1. *Crystallographic data and K-absorption edges*

	Cu_2O*	TiO_2†	MnF_2‡
	Cubic	Tetragonal	
a_0 (Å)	4·2696	4·59366	4·8734
c_0 (Å)		2·95868	3·3099
V (Å^3)	77·773	62·435	78·610
Space group	$Pn\bar{3}m$ (No. 224)	$P4_2/mnm$ (No. 136)	
Z	2	2	
Atoms	Cu 4(*b*) (0, 0, 0; $\bar{3}m$)	Me 2(*a*) (0, 0, 0; *mmm*)	
	O 2(*a*) ($\frac{1}{4},\frac{1}{4},\frac{1}{4}$; $\bar{4}3m$)	F, O 4(*f*) ($x, x, 0$; $x \simeq 0{\cdot}3049$; *mm*)	
K edge (Å)	1·38059	2·49734	1·89643
(keV)	8·9803	4·96452	6·5376

* Kirfel & Eichhorn (1990).
† Restori & Schwarzenbach (1987).
‡ Jauch, Schultz & Schneider (1989).

Crystal structures and samples

Crystallographic data for cubic Cu_2O and tetragonal TiO_2 and MnF_2 are summarized in Table 1.

Semi- and photoconducting cuprite has attracted much interest by both experimental crystallographers and theoreticians. The structure including the electron deformation density distribution has been well determined, recently by Kirfel & Eichhorn (1990). The outstanding feature is a perfectly linear and symmetric O–Cu–O arrangement [Fig. 2(*a*), Cu–O

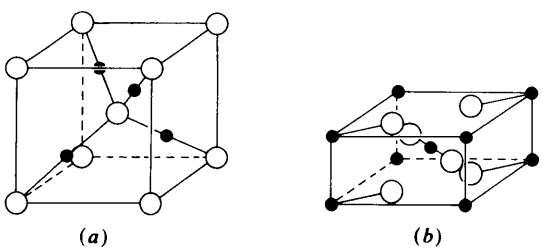

(*a*) (*b*)

Fig. 2. Crystal structures of (*a*) cuprite (origin at $\bar{4}3m$) and (*b*) rutile. The metal atoms are indicated by full spheres.

1·848 Å] requiring a considerable amount of covalent bonding. Owing to this anisotropic chemical environment of Cu, one can intuitively expect anisotropy of the X-ray susceptibility at resonance energies. Theoretical calculations by Nagel (1985) and Marksteiner, Blaha & Schwarz (1986) indicated a Cu d^8 plus doubly occupied $3d_{z^2}$–$4s$ hybrid state. The band-structure calculations of the latter authors yielded two close peaks in the DOS of the p band (mainly due to O $2p$ states) which correspond to a large unresolved peak (6–7 eV below E_F) in the photoelectron spectrum reported by Thuler, Benbow & Hurych (1982). Thus, excitation of Cu K electrons into this (these) p state(s) is likely for K-absorption-edge energies.

The point symmetry of the Cu site is $\bar{3}m$ allowing symmetric $\mathbf{f}'$ and $\mathbf{f}''$ tensors, each with equal diagonal ($f_{11}=f_{22}=f_{33}$) and off-diagonal ($f_{12}=f_{13}=f_{23}$) elements, respectively. Since, according to (15) and (16), the former elements do not contribute to 'forbidden' reflection intensities, there is only one complex parameter, f_{12}, to be considered in the structure-factor tensor $\mathbf{F}(\mathbf{h})_a$. Owing to the cubic symmetry, absorption is isotropic so that diffraction is the only way to (i) obtain direct proof of the excitation of $1s$ electrons into a p state, and (ii) assess the magnitude of the resulting anisotropy in the anomalous dispersion of Cu.

Another interesting feature of the cuprite structure is the division of the allowed reflections into four parity classes, (*eee*), (*ooo*), (*ooe*) and (*eeo*). If contributions of aspherical atomic density distributions due to chemical bonding are neglected, the (*eeo*) reflections are 'forbidden' by the special atom positions, and the (*ooe*) reflections are weak, being determined by the O atoms alone. Thus, besides the systematically extinct zonal reflections ($hk0$; $h+k=2n+1$), these reflections are, in keeping with (16), of particular interest for tests of the scattering model.

Samples of Cu_2O were prepared from two natural batches from Canada, hereafter referred to as CUC, and Western Australia, CUA. From CUC we have taken the crystal sphere (0·173 mm diameter) already used in our electron-density study (Kirfel & Eichhorn, 1990) and a crystal cube of $6\times5\times4{\cdot}5$ mm cut perpendicular to $[0\bar{1}1]$, [111] and $[2\bar{1}\bar{1}]$. Both crystals were regularly mounted on goniometer heads. From CUA, thin slinces of 20×20 mm were cut perpendicular to [100] and [110] and polished to about 40 μm. In order to ensure mechanical stability these wafers were then glued to thin glass plates which could be mounted as usual.

The rutile structure compounds, TiO_2 and MnF_2, were chosen for the following reasons:

(i) Like cuprite, rutile has been investigated in numerous studies concerning the bonding character and its relation with its extraordinary physical properties (Abrahams & Bernstein, 1971; Gonschorek, 1982). The structures are well determined (TiO_2: Restori & Schwarzenbach, 1987; MnF_2: Jauch, Schultz & Schneider, 1989) and large crystals are available.

(ii) Polarization dependence of the photoelectric absorption coefficient has been observed for isotypic ZnF_2 at the Zn K-absorption edge by Cox & Beaumont (1980). Particularly for the 'white line' which is associated with a high density of states with p symmetry above the Fermi level they reported an anisotropy of μ of up to 25%. This finding means AAD for Zn, and similar conditions could be expected for the Ti and Mn cations.

(iii) This possibility has been discussed in detail by Dmitrienko (1983). Though the metal atom is coordinated by an almost regular oxygen octahedron (Ti–O 1·980 and 1·948; Mn–F 2·102 and 2·132 Å), the structure can also be imagined as being constructed from successive layers of O–Ti–O entities (compare O–Cu–O) directed alternately at 45 and −45° to the a_0 axis (Fig. 2*b*). The principal axes of the $\mathbf{f}'$ and $\mathbf{f}''$ tensors for subsequent layers are therefore orthogonally oriented, allowing the occurrence of 'forbidden' reflections. Thus, experimental verification of Dmitrienko's prediction was one aim of our investigation.

The TiO_2 sample was a large natural prism of 14×14 mm cross section from Steiermark, Austria. The prism faces were {100} and {110} and the (001) face was obtained by cutting the crystal. Owing to lack of time, the faces received no further treatment.

For MnF_2, a synthetic crystal plate ($15\times10\times2$ mm) with polished (100) faces was kindly provided by W. Jauch (Hahn-Meitner-Institut, Berlin, Germany).

Experimental

All experiments were carried out during dedicated beam time, *i.e.* DORIS II being operated at 3·7 GeV, critical energy 9 keV, maximum injected current 100 mA. This mode of operation provides in general stable beam conditions and fills lasting up to 4 h. For the majority of the measurements on the large specimens we have used the two-axis diffractometer installed at beam line G3 at HASYLAB (Bonse & Fischer, 1981). Supplementary measurements on the Cu_2O crystal sphere were performed on the six-circle diffractometer installed at line C (Bondza, Hümmer & Weckert, 1986; Hümmer, Weckert & Bondza, 1989). This instrument allows true Ψ rotations around the scattering vector (without mechanical limitations) and is operated as fast and almost as comfortably as a four-circle machine.

At both diffractometers, the radiation was monochromatized by symmetric flat double-crystal arrangements [two-axis: Si(111), six-circle: Ge(111)] with fixed exits ($\Delta E/E\simeq4\times10^{-4}$). Contaminations of the radiation by third- and fourth-order harmonics

were carefully checked and, if necessary, reduced to negligible importance by both slightly detuning the monochromator and adjusting the energy discrimination of the counting chain.

Two-axis diffractometer

The experimental set-up used for all measurements on this instrument is depicted in Fig. 3. Bragg intensities were obtained by reflection from extended crystal faces. Normally, the scattering plane was vertical, however, the instrument allows also any other orientation of the scattering plane between vertical and horizontal since the diffractometer set-up indicated in Fig. 3 is mounted on a swing which can be rotated around the beam axis. Optimal homogeneity of the primary radiation was achieved by selecting a suitable cross section, *e.g.* 2×1 mm, from a $10\times$ 10 mm beam entering the monochromator.

Each crystal was mounted with the illuminated face under consideration perpendicular to the φ axis of a κ goniometer so that a Ψ rotation around the scattering vector **h** was accomplished by the φ circle. In order to exclude errors due to crystal misalignments, which were difficult to correct for, each intensity $I(\mathbf{h};\Psi)$ was determined from an ω scan at fixed Ψ. For each ω step, the ratio of the count rates provided by the NaI scintillation detectors measuring the diffracted radiation and monitoring the incident radiation (Petcov, Kirfel & Fischer, 1990) was fed into subsequent channels of a multichannel analyzer which provided both an on-line graphics display of the normalized peak profile and the total integrated intensity upon activating the integration mode. Thus, the Ψ-scan results reported below are based on relative and unreduced integrated intensities *vs* Ψ settings rather than count rates *vs* Ψ rotation.

The same ω-scan technique was also applied in the initial investigations of the energy dependence of the 'forbidden' reflection intensities in order to detect the resonance effects at the absorption edge and to optimize the intensity yield. Thus, the experimental procedure carried out for each compound comprised generally the following steps:

(1) Calibration of the monochromator by measurement of the respective *K*-absorption edges. This was achieved by either absorption measurements on powdered samples or by observing the energy dependence of an allowed reflection in combination with fluorescence measurements. The near-edge region was then fine scanned with energy increments of about 10 eV in order to establish the energy range to be covered in the ensuing search for 'forbidden' reflections.

(2) After proper crystal alignment, based on at least two allowed reflections, crystal and detector were positioned to the calculated settings for a 'forbidden' reflection, and the energy was again varied over the absorption edge using increments ΔE between 1·5 and 5 eV. When possible, the correct settings for the Bragg condition were confirmed by tuning the monochromator to maximum output of the fourth order and registering the intensity of the corresponding allowed reflection. Since the 'energy scans' were rather time consuming and sensitive on the beam stability, the choice of the energy increments depended on the developing picture. Mainly due to lack of time, these scans were therefore not intended to yield spectra of the highest possible resolution and reliability, but served rather to determine the resonance energy to be used for the subsequent polarization-dependent intensity measurements.

(3) These were performed varying Ψ between 0 and π or 2π, respectively, with $5\leq\Delta\Psi\leq15°$ and ω-scan ranges adapted to the actual peak profiles which varied considerably with the crystal quality. The number of profile points was between 51 and 91, and each point was measured for at least 10 s. Including the time for the circle movements, each ω scan required therefore between 12 and 22 min yielding about 10–20 $I(\mathbf{h};\Psi)$ values per run, for an optimal performance of DORIS II.

Finally, in many experiments, *e.g.* for MnF_2, we have also recorded the fluorescence yield using a third detector at $2\Theta=90°$ looking down on the reflecting crystal face.

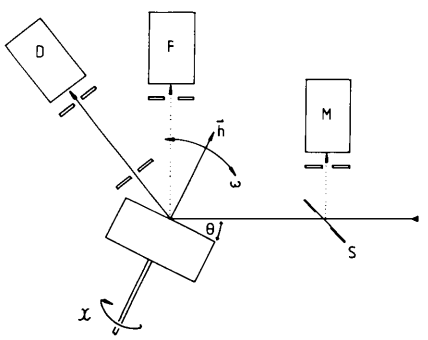

Fig. 3. Experimental set-up on the two-axis diffractometer (S = scattering foil; M, F, D = NaI detectors for monitorization, fluorescence yield and diffracted beam).

Six-circle diffractometer

The additional measurements on the Cu_2O sphere (CUC) were carried out in order to (i) check the results obtained on the above instrument, (ii) test the feasibility of a faster experiment on a much smaller scattering volume (*i.e.* conventional diffractometry) and (iii) be free in the choice of reflections to be investigated. In particular, the latter point was of interest in view of testing the scattering model on some allowed reflections.

The measurements were conducted using the bathing method, with vertical scattering geometry, and

with primary-beam monitorization as described before. After establishment of the orientation matrix and optimization of the radiation energy, normalized $I(\mathbf{h};\Psi)$ functions were again evaluated from sequences of individual ω scans at increasing azimuthal angles ($3 \le \Delta\Psi \le 15°$). These scans consisted of 200 profile points ($\Delta\omega = 0{\cdot}003°$), each measured for 1 s. The determination of a single value $I(\mathbf{h};\Psi)$ took therefore less than 4 min, being at least three times faster than before, and a full Ψ rotation comprising 37 experimental points could be completed within about 150 min.

Results and discussion

In this section, the scattering model is applied to the cuprite- and rutile-type structures. Intensity functions are explicitly formulated for selected reflections and are then compared on a relative scale with experimental results. Fits of the model curves to the observations were carried out using the program *MINUIT* (James & Roos, 1987). A list of the experiments is given in Table 2.

Cuprite, Cu_2O

Owing to the Cu atom's site symmetry $\bar{3}m$, the allowed scattering-factor tensor **f** possesses only one unique complex off-diagonal element f_{12}.

Model predictions

(*a*) '*Forbidden*' *reflections* $hk0$, $h+k=2n+1$. For systematically extinct zonal reflections $hk0$ with odd h and even k, and including the temperature factor in f_{12}, $\mathbf{F}(\mathbf{h})_{Ca}$ of (15*a*) takes the form

$$\mathbf{F}(hk0)_{Ca} = 4f_{12}\begin{pmatrix}0&0&1\\0&0&0\\1&0&0\end{pmatrix}$$

and in the diffractometer system allowing also for a rotation around **h**:

$$\mathbf{F}(hk0;\Psi)_{Da} = 4f_{12}\begin{pmatrix}0 & -\sin\varphi\sin\Psi & -\sin\varphi\cos\Psi\\ -\sin\varphi\sin\Psi & 2\cos\varphi\sin 2\Psi & \cos\varphi\cos 2\Psi\\ -\sin\varphi\cos\Psi & \cos\varphi\cos 2\Psi & -\cos\varphi\sin 2\Psi\end{pmatrix}. \quad (33)$$

where $\varphi = \tan^{-1}(k/h)$. According to (28),

$$\begin{aligned}\Phi_{a\sigma'\sigma}(hk0;\Psi) &= -4f_{12}\cos\varphi\sin 2\Psi\\ \Phi_{a\pi'\sigma}(hk0;\Psi) &= -4f_{12}(\cos\Theta\sin\varphi\cos\Psi\\ &\quad +\sin\Theta\cos\varphi\cos 2\Psi)\\ \Phi_{a\sigma'\pi}(hk0;\Psi) &= -4f_{12}(\cos\Theta\sin\varphi\cos\Psi\\ &\quad -\sin\Theta\cos\varphi\cos 2\Psi)\\ \Phi_{a\pi'\pi}(hk0;\Psi) &= -4f_{12}\sin^2\Theta\cos\varphi\sin 2\Psi.\end{aligned} \quad (34)$$

Table 2. *List of the near-edge diffraction experiments*

The investigated dependencies of the reflection intensities are indicated (for details see text).

Instrument	Sample	Reflection	Fig.
Two-axis diffractometer	Cu_2O (CUC) Crystal cube	$I(005; E; \kappa)$	4(*a*)
	Cu_2O (CUA) (100) wafer	$I(100;\Psi)$	5(*a*)
		$I(300;\Psi)$	5(*b*)
		$I(500;\Psi)$	5(*c*)
		$I(200;\Psi)$	7(*a*)
	(110) wafer	$I(330;\Psi)$	7(*b*)
Six-circle diffractometer	Cu_2O (CUC) Crystal sphere	$I(100;\Psi)$	5(*d*)
		$I(300;\Psi)$	5(*e*)
		$I(120;\Psi)$	6(*a*)
		$I(140;\Psi)$	6(*b*)
		$I(320;\Psi)$	6(*c*)
		$I(330;\Psi)$	7(*c*), (*d*)
Two-axis diffractometer	TiO_2 Natural prism	$I(100; E)$	8(*a*)
		$I(100;\Psi)$	8(*b*)
		$I(001;\Psi)$	8(*c*)
	MnF_2 Synthetic plate	$I(100; E)$	9(*a*)
		$I(100;\Psi)$	9(*b*)

(Note that $\Phi_{a\pi'\sigma} \neq \Phi_{a\sigma'\pi}$.) Inserting these results into (16) one obtains, for elliptically polarized incident radiation,

$$\begin{aligned}I(hk0;\Psi) &\propto 16|f_{12}|^2[(|A_{0\sigma}|^2+\sin^4\Theta|A_{0\pi}|^2)\cos^2\varphi\sin^2 2\Psi\\ &\quad +(|A_{0\sigma}|^2+|A_{0\pi}|^2)(\cos^2\Theta\sin^2\varphi\cos^2\Psi\\ &\quad +\sin^2\Theta\cos^2\varphi\cos^2 2\Psi)+(|A_{0\sigma}|^2-|A_{0\pi}|^2)\\ &\quad \times 0{\cdot}25\sin 2\Theta\sin 2\varphi\cos\Psi\cos 2\Psi].\end{aligned} \quad (35)$$

Note that for σ- or π-polarized radiation and reflections $h00$, (35) is consistent with (24) of Dmitrienko (1983).

As pointed out in the discussion of (21), the mixed term of (17), $I_{\sigma\pi}$, vanishes since $f'_{12} \propto f''_{12}$. Equation (35) was developed in detail in order to show the geometrical depencencies and, in particular, to emphasize that, even for intensity measurements on an absolute scale, the 'forbidden' reflections can only yield $|f_{12}|^2 = f'^2_{12} + f''^2_{12}$, but not the individual contributions, f'_1 and f''_{12}. These can be assessed only from an allowed reflection.

Taking SR with a reasonable estimate of $|A_{0\pi}|^2 = p|A_{0\sigma}|^2$, $p \simeq 0{\cdot}05$ corresponding to 91% linear polarization in the horizontal plane, (35) allows the following predictions for axial reflections $h00$ with $\varphi = 0$:

(i) $I(h00;\Psi)$ will peak at $\Psi = \pm\pi/4$ and $\pm 3\pi/4$ with maxima proportional to $|f_{12}|^2(1+p\sin^4\Theta) \simeq |f_{12}|^2$ for practical scattering angles.

(ii) $I(h00;\Psi)$ shows minima at $\Psi = 0, \pm\pi/2, \pi$ proportional to $|f_{12}|^2(1+p)\sin^2\Theta$. Thus, each 'forbidden' reflection intensity possesses a Ψ-invariant component which increases with increasing scattering angle and approaches $|f_{12}|^2$ for the backscattering case.

(iii) The degree of σ polarization can be calculated from (10) and takes a complicated form. For the maxima and minima, however, $P_{\Theta\sigma}$ reduces to $P_{\Theta\sigma} = 1/(1+p\sin^4\Theta)$ and $P_{\Theta\sigma} = p/(1+p)$, respectively. Thus, for small scattering angles the polarization remains almost unchanged at maximum scattering, whereas the diffracted beam is almost totally π polarized at the minima.

(iv) The intensity modulation is characterized by $I_{min}/I_{max} \simeq \sin^2\Theta$ for small p.

(*b*) *Allowed reflections hk*0. In order to show how AAD can affect allowed reflections and that, in particular, the anisotropy of the real and imaginary parts of the anomalous dispersion are accessible from allowed reflections, the weak 'oxygen' reflections *hk*0 with both *h* and *k* odd will be considered. From (15) and (30)-(32) follows

$$\mathbf{F}(hk0;\,\Psi)_{Da} = 4f_{12}\begin{pmatrix} -\sin 2\varphi & \cos 2\varphi\cos\Psi & -\cos 2\varphi\sin\Psi \\ \cos 2\varphi\sin\Psi & \sin 2\varphi\cos^2\Psi & -0{\cdot}5\sin 2\varphi\sin 2\Psi \\ -\cos 2\varphi\sin\Psi & -0{\cdot}5\sin 2\varphi\sin 2\Psi & \sin 2\varphi\sin^2\Psi \end{pmatrix} \quad (36)$$

and

$$\Phi_{a\sigma'\sigma}(hk0;\,\Psi) = 4f_{12}\sin 2\varphi\sin^2\Psi$$

$$\Phi_{a\pi'\sigma}(hk0;\,\Psi) = 4f_{12}(0{\cdot}5\sin\Theta\sin 2\varphi\sin 2\Psi - \cos\Theta\cos 2\varphi\sin\Psi). \quad (37)$$

For σ-polarized radiation, with $F_0 = A_0 + iB_0$, (16) yields:

$$I(hk0;\,\Psi) \propto |F_0|^2 + 8(A_0f'_{12} + B_0f''_{12})\sin 2\varphi\sin^2\Psi + 16|f_{12}|^2[\sin^2 2\varphi\sin^4\Psi + (0{\cdot}5\sin\Theta\sin 2\varphi\sin 2\Psi - \cos\Theta\cos 2\varphi\sin\Psi)^2], \quad (38)$$

showing for all $\Psi \neq 0$ or π an addition of intensity to $|F_0|^2$ which depends only little on the scattering angle Θ. When the real and imaginary components of the structure factor are known, not only the magnitude of the effect but also both f'_{12} and f''_{12} can be determined from relative intensity measurements and a fit of (38) to the observations. This applies, of course, also to elliptically polarized SR. The expression for $I(hk0;\,\Psi)$ is considerably more complicated, however.

(*c*) *Rotation of scattering plane.* Another point of consideration concerns the rotation (κ) of the scattering plane around the incident beam, which is equivalent to a rotation of the polarization directions. If one assumes, for simplicity, that the radiation is σ polarized, then

$$|A_{0\sigma}|^2 \propto \sin^2\kappa \quad \text{and} \quad |A_{0\pi}|^2 \propto \cos^2\kappa$$

and (35) yields for $\Psi = \pi/4$ (intensity maximum):

$$I(h00;\,\pi/4;\,\kappa) \propto \sin^2\kappa + \sin^4\Theta\cos^2\kappa. \quad (39)$$

The relative intensity should thus decrease from 1 to $\sin^4\Theta$ upon changing the scattering plane from vertical to horizontal.

Experimental results

(*a*) *Energy scans and rotation of the scattering plane.* Fig. 4(*a*) shows the energy dependence of the 'forbidden' reflection 500 below and at the Cu K-absorption edge ($\Theta \simeq 54°$). These measurements were performed on the two-axis diffractometer by observing the equivalent intensity $I(005)$ reflected from the (011) face of the crystal cube (CUC) at $\Psi = 45°$. They were basically intended to provide an initial proof of the occurrence of FRED in Cu_2O. Recording these spectra for five orientations of the scattering plane was very time consuming, since each observation required an energy change and realignment of crystal and detector. Though care was taken to illuminate the same area for all κ settings, this could not be

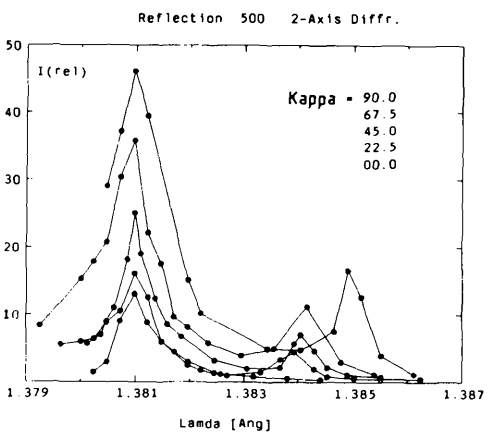

(*a*)

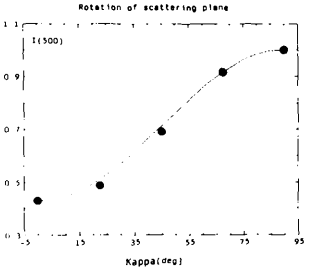

(*b*)

Fig. 4. Cuprite. (*a*) κ dependence of the observed maximum intensities of $I(500)$ compared to the model curve. (*b*) Rotation of the scattering plane. Sequence of relative intensities $I(500)$ at $\Psi = 45°$ as functions of energy. The largest peak corresponds to the vertical scattering plane ($\kappa = 90°$), the smallest to the horizontal ($\kappa = 0°$). The Cu *K*-absorption edge is at 1·3806 Å.

checked rigorously. In the course of the experiments it turned out that the special construction of the instrument caused a further problem. Since the monochromator box is attached to the frame carrying the swings, rotations of the swings lead to shifts in the energy calibration (which would be avoided by a stand-alone monochromator unit). This behavior results in uncertainties in the energy scales associated with each spectrum. In Fig. 4(*a*) we have plotted the spectra with the main peaks occurring at the same energy which may, however, be incorrect.

In spite of these experimental difficulties connected with the rotation of the scattering plane, the observations yield a consistent picture. For $\kappa = 90°$, *i.e.* a vertical scattering plane, the spectrum shows two distinct resonance peaks separated by about 30 eV. The smaller peak is well below the absorption edge and may be associated with a bound excited state. Upon rotation towards horizontally scattering this peak decreases to zero accompanied by a shift to higher energies. The main peak also decreases with decreasing κ and reproduces clearly the trend predicted by (39) for $E =$ constant. Fig. 4(*b*) compares (39) to the observed maximum intensities as a function of κ, after applying a linear correction $I_c = I_{obs}(0{\cdot}1335 - 517 \times 10^{-4}\,\kappa)$. Though the origin of this correction is not fully understood, we consider the agreement in Fig. 4(*b*) as a satisfactory confirmation of (39).

(*b*) *Ψ rotations for 'forbidden' hk0 reflections.* In order to exclude systematic errors in a rigorous check of the scattering model, these measurements were carried out on two samples and on two different instruments. On the two-axis diffractometer $I(h00; \Psi)$ was determined by reflection from a (100) wafer (CUA). On the six-circle diffractometer, we have used the small crystal sphere (CUC). The observed relative intensities of the reflections 100, 300 and 500 are shown in Figs. 5(*a*)-(*e*). (Reflection 700 is already outside the Ewald sphere, $\lambda = 1{\cdot}38$ Å.) Least-squares fits of (35) yielded agreement indices between 4 and 12% for $p = 0$. The discrepancies between the model curves and the observations are mainly due to small energy variations occurring predominantly at the end of a SR run. Occasionally, multiple scattering (*Umweganregung*) was observed which is readily recognized from dramatically increased intensities. Corresponding data were omitted from the fits.

Fig. 5(*f*) shows the dependence of the intensity modulations, *i.e.* I_{min}/I_{max}, on $\sin^2\Theta$. The calculated curves correspond to σ-polarized ($p = 0$) and elliptically polarized radiation ($p = 0{\cdot}05$), respectively, the latter showing excellent agreement with the observations for $I(500)$.

The scattering model is also in agreement with the observed intensity variations of the 'forbidden' zonal reflections 120, 140 and 320 which were measured on the six-circle diffractometer. The results are plotted in Fig. 6 together with the model curves obtained from fits of (35) for σ-polarized radiation ($p = 0$). The agreement indices were $R = 0{\cdot}079$, $0{\cdot}09$ and $0{\cdot}069$, respectively.

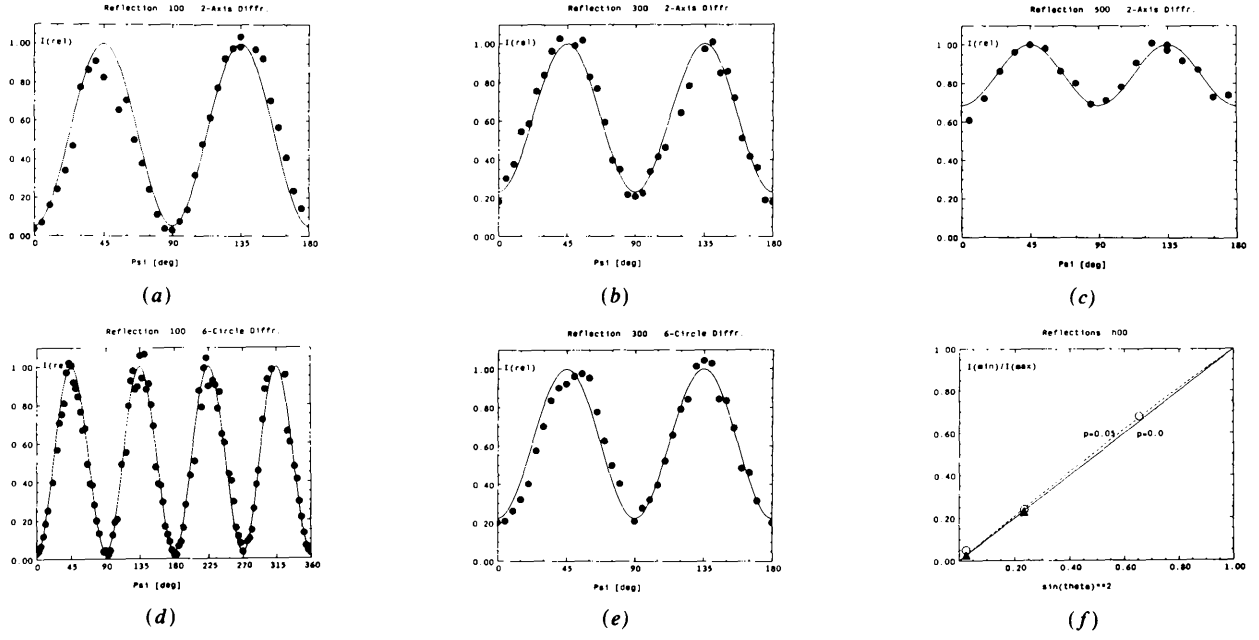

Fig. 5. Cuprite: Intensity variations upon Ψ rotation around the scattering vector and fits of model functions for 'forbidden' *h*00 reflections. (*a*), (*b*), (*c*) Two-axis diffractometer, sample CUA. (*d*), (*e*) Six-circle diffractometer, sample CUC. (*f*) I_{min}/I_{max} *vs* $\sin^2\Theta$ compared to model curves.

An encouraging outcome of these experiments is the data quality obtained on the six-circle diffractometer for a sample volume of only 0·0027 mm^3. In agreement with Templeton & Templeton (1985*a*, 1986, 1987), Figs. 5(*d*), (*e*) and 6(*a*)-(*c*) demonstrate clearly that a 'normal' size crystal can exhibit effects that can be well measured (and exploited) on any single-crystal diffractometer installed at an intense X-ray radiation source.

(*c*) Ψ *rotations for allowed reflections.* For the allowed reflections $h00$ with even h, one finds from (15) that $\mathbf{F}(h00)_a$ equals zero. Thus, $\mathbf{I}(200; \Psi)$ must be invariant to rotation around the scattering vector. This was checked in the course of the experiments with the (100) CUA wafer. The result is shown in Fig. 7(*a*) which proves also that the intensity modulations of the 'forbidden' reflections are not caused by a systematic error in the experimental procedure. Fig. 7(*a*) contains the original observations on a relative scale, the mean value and the e.s.d. calculated from the scatter. The observed drift in $I(200; \Psi)$ may be partly due to neglecting the dead-time correction in the intensity normalization and/or an energy shift (beam displacement) in the course of the SR run. It should also be noted that multiple scattering occurred at $\Psi = 40°$ and the storage ring was refilled at $\Psi = 140°$.

The intensity variations of the 'oxygen' reflection 330 are given in Figs. 7(*b*)-(*d*). The results from the (110) wafer (sample CUA) in Fig. 7(*b*) as well as from the crystal sphere (CUC) in Figs. 7(*c*), (*d*) show a considerable π-periodic Ψ dependence of the 330 intensity. For isotropic anomalous dispersion of Cu, $I(330)$ depends exclusively on the oxygen scattering factor. Again, Fig. 7(*c*) contains the original data displaying the influence of energy drifts and/or imperfect normalization. These effects can, however,

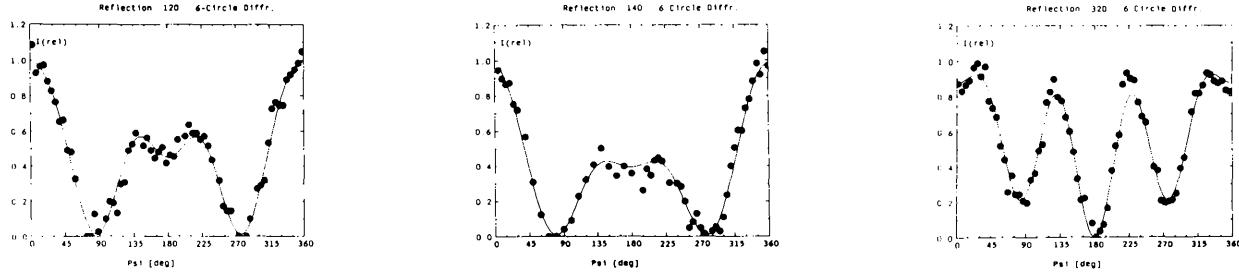

(*a*) (*b*) (*c*)

Fig. 6. Cuprite: Ψ dependencies of intensities and fits of model functions for 'forbidden' $hk0$ reflections. Six-circle diffractometer, sample CUC.

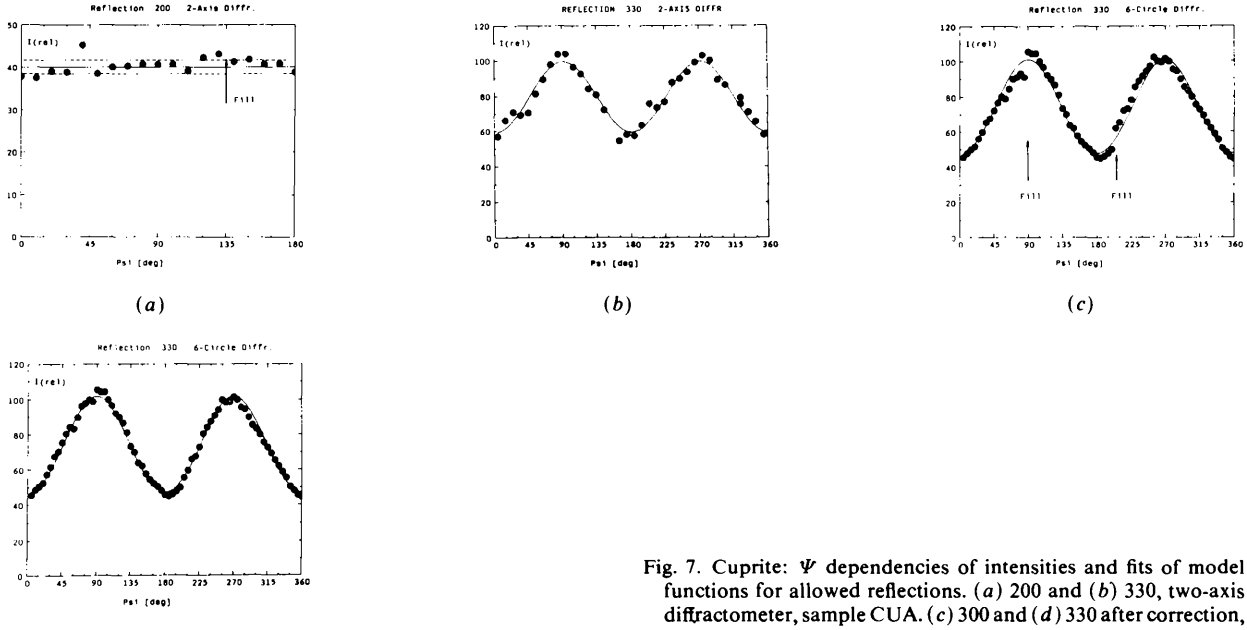

(*a*) (*b*) (*c*)

(*d*)

Fig. 7. Cuprite: Ψ dependencies of intensities and fits of model functions for allowed reflections. (*a*) 200 and (*b*) 330, two-axis diffractometer, sample CUA. (*c*) 300 and (*d*) 330 after correction, six-circle diffractometer, sample CUC.

be eliminated by linear corrections as shown in Fig. 7(*d*).

The almost-equal isotropic thermal-vibration amplitudes of Cu and O ($B = 1{\cdot}5$ Å^2; Kirfel & Eichhorn, 1990) allow estimates of f'_{12} and f''_{12} from fits of (35) to the observations. With $A_0(330) = -2[f(\mathrm{O}) + 0{\cdot}04]$ and $B_0(330) = 0{\cdot}054$ for $T = 0$ K, these resulted in $R = 0{\cdot}038$ (CUA; Fig. 7*b*) and 0·026 (CUC; Figs. 7*c*, *d*), respectively. The corresponding parameters were determined as $f'_{12} = -0{\cdot}35$ (4), $-0{\cdot}56$ (6) and $f''_{12} = -0{\cdot}23$ (54), 0·0(5). The differences can be attributed to different photon energies. Since the experiments on the CUA wafers were at the same energy, the results obtained for 330 (CUA), $|f_{12}|^2 = 0{\cdot}0824$ [e^2] for room temperature, could be cross checked against $I(100)_{\max}/I(200)$. After Lorentz and filter corrections for $I(200)$, $|F(100, \Psi)|^2_{\max} = 1{\cdot}30$ yielding $|f_{12}|^2 = 0{\cdot}081$ [e^2] from (35). In view of the large e.s.d. of f''_{12} (due to the small B_0) this agreement may be fortuitous. However, the magnitude and sign of f'_{12} are determined in fair agreement from the two different experiments on different samples. These quantitative results indicate that the AAD in cuprite can amount to 10–20% of the isotropic anomalous-dispersion correction terms, an effect that cannot be neglected in the evaluation of near-edge diffraction data.

Rutile-type TiO_2 *and* MnF_2

The experiments on TiO_2 and MnF_2 were intended to provide additional checks of the scattering model. They were performed exclusively on the two-axis diffractometer.

As for cuprite, the scattering-factor tensor **f** of the metal atom in (0, 0, 0; *mmm*) is symmetric and possesses one unique off-diagonal element f_{12}, however, $f_{13} = f_{23} = 0$.

Model predictions for 'forbidden' reflections h0l

Following the same procedure as before, one obtains for the systematically extinct zonal reflections *h0l* with $h + l = 2n + 1$:

$$\mathbf{F}(h0l)_{Ca} = 2f_{12}\begin{pmatrix} 0 & 1 & 0 \\ 1 & 0 & 0 \\ 0 & 0 & 0 \end{pmatrix}$$

and

$$\begin{aligned}
\Phi_{a\sigma'\sigma}(h0l;\,\Psi) &= 2f_{12}\sin\chi\sin 2\Psi \\
\Phi_{a\pi'\sigma}(h0l;\,\Psi) &= -2f_{12}(\cos\Theta\cos\chi\sin\Psi \\
&\quad -\sin\Theta\sin\chi\cos 2\Psi) \\
\Phi_{a\sigma'\pi}(h0l;\,\Psi) &= -2f_{12}(\cos\Theta\cos\chi\sin\Psi \\
&\quad +\sin\Theta\sin\chi\cos 2\Psi) \\
\Phi_{a\pi'\pi}(h0l;\,\Psi) &= 2f_{12}\sin^2\Theta\sin\chi\sin 2\Psi.
\end{aligned} \tag{40}$$

These equations resemble (34) expressing once more the geometric aspect. Since $\chi = \pi/2$ for 00*l* and $\chi = 0$ for *h*00, $\Phi_{a\sigma'\sigma}(h00) = \Phi_{a\pi'\pi}(h00) = 0$, *i.e.* the diffracted beam of an *h*00 reflection is polarized orthogonally to the incoming one [see (22)].

Using again only σ-polarized radiation, one gets

$$\begin{aligned}
&I(h0l;\,\Psi) \\
&\quad \propto 4|f_{12}|^2[\sin^2\chi\sin^2 2\Psi + (\cos\Theta\cos\chi\sin\Psi \\
&\qquad -\sin\Theta\sin\chi\cos 2\Psi)^2].
\end{aligned} \tag{41}$$

For the axial reflections, (41) simplifies to

$$I(h00;\,\Psi) \propto 4|f_{12}|^2\cos^2\Theta\sin^2\Psi \tag{42}$$

$$I(00l;\,\Psi) \propto 4|f_{12}|^2(\sin^2\Theta + \cos^2\Theta\sin^2 2\Psi). \tag{43}$$

Again, the 'forbidden' reflections can only give information about $|f_{12}|$. Equation (43) is in agreement with Dmitrienko (1983) and equals $I(00l;\,\Psi)$ for cuprite, both reflecting the fourfold symmetries of the structures (Fig. 2) projected along [001].

Experimental results

Figs. 8(*a*) and 9(*a*) show the energy dependencies of the reflections 100 at $\Psi = 90°$, giving us the optimal energy settings for the subsequent Ψ rotations. It is

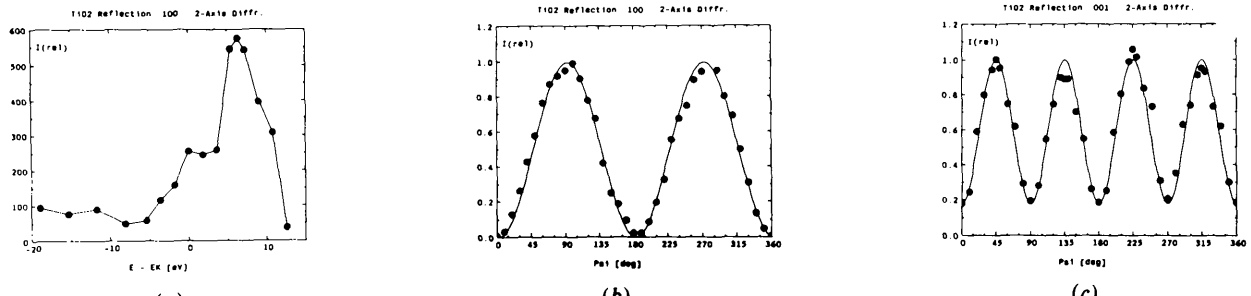

(*a*) (*b*) (*c*)

Fig. 8. Rutile TiO_2, two-axis diffractometer. (*a*) Energy dependence of 'forbidden' reflection 100 at $\Psi = 90°$; (*b*) and (*c*) Ψ dependencies of intensities and fits of model functions for reflections 100 and 001, respectively.

interesting to note that in case of MnF_2 a logarithmic plot of the more-extended measurements reveals at least three resolved resonance peaks of which the two smaller ones are already in the EXAFS region. Estimates of the FWHM of the main peaks in Figs. 8(*a*) and 9(*a*) yield a common result, about 7 eV compared to 10 eV for cuprite (Fig. 4*a*).

The intensity distributions $I(100; \Psi)$ are shown in Figs. 8(*b*) and 9(*b*) together with fits of (42) giving agreement indices of $R = 0{\cdot}066$ and 0·078, respectively. An example of $I(001; \Psi)$ and a fit of (43), $R = 0{\cdot}077$, is given in Fig. 8(*c*) for TiO_2. Similar to cuprite the ratio I_{min}/I_{max} is predicted to vary with $\sin^2 \Theta$. The ratio from the fit curve, 0·19, compares satisfactorily with the calculated value of 0·178.

Finally, Fig. 9(*c*) shows an example of the fluorescence yield obtained during a Ψ rotation. For cubic cuprite and the 001 reflection of tetragonal MnF_2, these measurements displayed no significant Ψ dependence in agreement with expectation, since absorption must be isotropic. The rotation around [100], however, gives a clear anisotropy of the fluorescence and consequently of the photoelectric absorption in accordance with the crystal symmetry. From the intensity pattern of Fig. 9(*c*) one can infer that $\mu_{\parallel c} = 0{\cdot}85\ \mu_{\parallel a}$ at 5 eV above the *K*-absorption edge of Mn. As a matter of fact, this anisotropy of absorption affects the intensity of the incoming beam, but hardly affects the diffracted outgoing beam because $\Phi_{a\sigma'\sigma}(h00) = 0$ and $\cos \Theta_{(100)} = 0{\cdot}958$. In a quantitative analysis, this absorption effect would have to be corrected for. In the present qualitative study, however, the Ψ dependence of $I(100)$ and of an absorption correction are the same so that the observed pattern remains unaffected on the relative scale.

Concluding remarks

A general model of kinematic Bragg diffraction in crystals exhibiting AAD of an absorbing element was developed on the basis of:

(i) atomic scattering-factor tensors which are compatible with the 'edge' atom's site symmetry; and

(ii) the Jones formalism which provides a convenient description of the radiation properties of both incident and diffracted beams.

Though the theoretical part of this study is closely related to the work by Templeton & Templeton and Dmitrienko, it offers for the first time a concise and general treatment of the dependence of the diffraction effects on both intensity and polarization. The model is valid for both polarized and unpolarized incident radiation. The algorithm uses conventional crystallographic nomenclature and refers to conventional four-circle single-crystal diffractometry. It is therefore a straightforward task to program an intensity calculation routine. The more involved incorporation of the model into a least-squares program which allows for the refinement of the **f**′ and **f**″ tensor elements from diffraction data $I(\mathbf{h}; \Psi)$ is under progress.

It is also noteworthy that the model allows for an antisymmetric component of the **f** tensor. Such a component is required, for example, for the understanding of space-group-extinct *hh.l* reflections ($l = 2n+1$) which have been observed in ferroelectric $LiNbO_3$ (Petcov, 1989). Predictions of diffraction from powder samples are readily obtained by integrating the intensity and polarization functions over all Ψ. The first evidence of the observability of FRED from Cu_2O powder was obtained by Kirfel, Eichhorn & Wroblewski (1988).

The energy dependence of 'forbidden' reflections in samples of cubic cuprite and tetragonal rutile type at the *K*-absorption edges of Cu, Ti and Mn give in each case clear evidence of excitation of unoccupied *p* states. Apart from proving that AAD occurs in both structure types, the calculated model predictions for $I(\mathbf{h}; \Psi)$ were verified for both 'forbidden' and allowed reflections. In all tests, the geometric dependencies were found to be strictly obeyed. Fits of explicit derived intensity functions to the observations yielded agreement indices between 0·04 to 0·10, giving credit to the model and indicating that data of

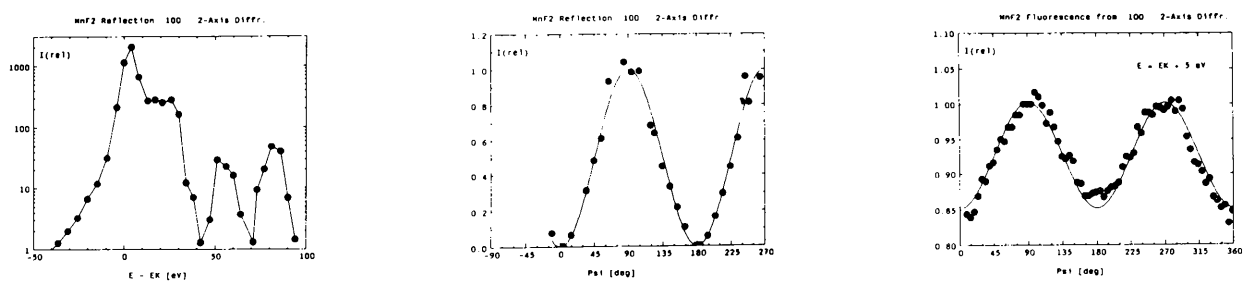

(*a*) (*b*) (*c*)

Fig. 9. Rutile-type MnF_2, two-axis diffractomer. (*a*) Energy dependence of 'forbidden' reflection 100 at $\Psi = 90°$ (note: I_{rel} on logarithmic scale). (*b*) As Fig. 8(*b*). (*c*) Ψ dependence and fit of model function for the fluorescence yield for the reflection 100, recorded at $2\Theta = 90°$.

sufficient quality can be obtained within reasonable time.

Though the 'forbidden' reflections were the main object of our experiments, it should be noted that the effect of AAD on allowed reflections can be appreciable, especially for weak reflections. The relative change of intensity that can occur upon rotation around the scattering vector can be estimated from the $hk0$ reflections in Cu_2O. For these, F_0 is almost real and $\Delta I/I \simeq \pm 8f'_{12}/F_0 + 16|f_{12}|^2$ which may easily exceed 100%. Since, in addition, the 'forbidden' reflections can only yield the modulus of the unique off-diagonal element of the complex **f** tensor [provided $I(\mathbf{h})_{\sigma\pi}$ of (20) vanishes], $I(\Psi)$ measurements of allowed reflections are the only way to assess its real and imaginary components separately. Thus, the weak reflections provide a rich source of information when the AAD is to be studied in detail and quantitatively.

The occurrence of significant AAD and FRED in the rutile structure compounds is an important and welcome result. Contrary to intuition, the effect does not require a considerably anisotropic environment for the 'edge' atom, as present in Cu_2O. This finding is encouraging with respect to studies on minerals, particularly rock-forming silicates, with small distortions of the coordination polyhedra of the cations. For these as for other substances FRED may be of interest, because it is highly selective: the signal stems exclusively from atoms of the absorbing element in the structure. Of these atoms only those contribute whose chemical bonding and site symmetry allow AAD. Thus, the signal is:

(i) undisturbed by the non-resonant scattering of the rest of the structure, regardless of its size and complexity;

(ii) proportional to the square of the number of contributing atoms;

(iii) periodic in Ψ with an intensity modulation that is determined by the geometrical factors G_{jk} in (13), *i.e.* it carries partial structure information.

These properties make FRED a potentially valuable tool in partial structure determination, in the study of order–disorder phenomena, and potentially in phase-transition and surface work. While for such applications the absolute magnitude of the effect and the energy resolution of the monochromator is of less importance, it is the energy stability of the incident radiation that counts most. Given, for example, a FWHM of the 'white line' of 10 eV as found for Cu_2O, and provided the energy is set to maximum resonance, an energy stability of ± 1 eV is required in order to operate with an intrinsic signal stability of $\pm 1{\cdot}5\%$. Under favorable conditions these figures can be met during the dedicated mode of DORIS II; however, this rarely occurs over hours or during the parasitic mode. The problem can, however, be alleviated by further improvements of beam steering as well as by higher primary-beam intensity speeding up the measurements.

Finally, the interested reader is reminded that the manifestation of AAD is not at all bound to the use of SR. Unpolarized radiation from a rotating-anode tube may be adequate for certain applications, provided sufficient intensity and/or magnitude of AAD. Thus, it may be well worth considering laboratory equipment for studies or applications of polarization-dependent resonant scattering.

This work has received financial support by the Bundesminister für Forschung und Technologie which is gratefully acknowledged. Our thanks are also due to Dr A. M. Glazer, University of Oxford, England, and Professor K. Langer, Technische Universität Berlin, Germany, for preparing the oriented thin cuts of cuprite, and to Dr E. Weckert, Universität Erlangen-Nürnberg, Germany, for help with the experiments on the six-circle diffractometer.

References

ABRAHAMS, S. C. & BERNSTEIN, J. L. (1971). *J. Chem. Phys.* **55**, 3206–3211.

BELYAKOV, V. A. & DMITRIENKO, V. E. (1989). *Sov. Phys. Usp.* **B32**(8), 697–719.

BONDZA, H., HÜMMER, K. & WECKERT, E. (1986). HASYLAB/DESY Jahresbericht, pp. 385–386. DESY, Hamburg, Germany.

BONSE, U. & FISCHER, K. (1981). *Nucl. Instrum. Methods*, **190**, 593–603.

BROUDER, C. (1990). *J. Phys. Condens. Matter*, **2**, 701–738.

BUSING, G. W. & LEVY, H. A. (1967). *Acta Cryst.* **22**, 457–464.

COX, A. D. & BEAUMONT, J. H. (1982). *Philos. Mag.* **B42**, 115–126.

DMITRIENKO, V. E. (1983). *Acta Cryst.* **A39**, 29–35.

DMITRIENKO, V. E. (1984). *Acta Cryst.*, **A40**, 89–95.

EICHHORN, K. & KIRFEL, A. (1988). *Z. Kristallogr.* **185**, 56–58.

GONSCHOREK, W. (1982). *Z. Kristallogr.* **160**, 187–203.

HÜMMER, K., WECKERT, E. & BONDZA, H. (1989). *Acta Cryst.* **A45**, 182–187.

JAMES, F. & ROOS, M. (1987). *MINUIT* program. Program Library No. D 506. CERN Computer Centre, Grenoble, France.

JAMES, R. W. (1982). *The Optical Principles of the Diffraction of X-rays*. Woodbridge, Connecticut: Ox Bow Press.

JAUCH, W., SCHULTZ, A. J. & SCHNEIDER, J. R. (1989). *J. Appl. Cryst.* **22**, 975–979.

JONES, R. C. (1941). *J. Opt. Soc. Am.* **31**, 488–493, 500–503.

JONES, R. C. (1948). *J. Opt. Soc. Am.* **38**, 671–685.

KIRFEL, A. & EICHHORN, K. (1988). HASYLAB/DESY Jahresbericht, pp. 265–266. DESY, Hamburg, Germany.

KIRFEL, A. & EICHHORN, K. (1989). HASYLAB/DESY Jahresbericht, pp. 383–384. DESY, Hamburg, Germany.

KIRFEL, A. & EICHHORN, K. (1990). *Acta Cryst.*, **A46**, 271–284.

KIRFEL, A., EICHHORN, K. & WROBLEWSKI, T. (1988). HASYLAB/DESY Jahresbericht, pp. 267–268. DESY, Hamburg, Germany.

KIRFEL, A. & PETCOV, A. (1989). HASYLAB/DESY Jahresbericht, pp. 385–386. DESY, Hamburg, Germany.

KIRFEL, A., PETCOV, A., FISCHER, K. & EICHHORN, K. (1988). HASYLAB/DESY Jahresbericht, pp. 263–264. DESY, Hamburg, Germany.

KIRFEL, A., PETCOV, A., JAUCH, W. & PALMER, A. (1989). HASYLAB/DESY Jahresbericht, pp. 387–388. DESY, Hamburg, Germany.

MARKSTEINER, P., BLAHA, P. & SCHWARZ, K. (1986). *Z. Phys.* B64, 119-127.
NAGEL, S. (1985). *J. Chem. Phys. Solids* 46, 743-756.
PETCOV, A. (1989). DESY F41. Internal Report 89-08. DESY, Hamburg, Germany.
PETCOV, A., KIRFEL, A. & FISCHER, K. (1990). *Acta Cryst.* A46, 754-763.
RESTORI, R. & SCHWARZENBACH, D. (1987). *Acta Cryst.* B43, 251-257.
TEMPLETON, D. H. & TEMPLETON, L. K. (1980). *Acta Cryst.* A36, 237-241.
TEMPLETON, D. H. & TEMPLETON, L. K. (1982). *Acta Cryst.* A38, 62-67.
TEMPLETON, D. H. & TEMPLETON, L. K. (1985*a*). *Acta Cryst.* A41, 133-142.
TEMPLETON, D. H. & TEMPLETON, L. K. (1985*b*). *Acta Cryst.* A41, 365-371.
TEMPLETON, D. H. & TEMPLETON, L. K. (1986). *Acta Cryst.* A42, 478-481.
TEMPLETON, D. H. & TEMPLETON, L. K. (1987). *Acta Cryst.* A43, 573-574.
TEMPLETON, D. H. & TEMPLETON, L. K. (1988). *Acta Cryst.* A44, 1045-1051.
THULER, M. R., BENBOW, R. L. & HURYCH, Z. (1982). *Phys. Rev. B*, 26, 669-677.

Acta Cryst. (1991). A47, 195-204

Solution of a Fab (26-10)/Digoxin Complex by Generalized Molecular Replacement

BY AXEL T. BRÜNGER

The Howard Hughes Medical Institute and Department of Molecular Biophysics and Biochemistry, Yale University, New Haven, CT 06511, USA

(*Received* 11 *July* 1990; *accepted* 22 *October* 1990)

Abstract

The structures of a Fab fragment of a monoclonal murine antidigoxin antibody (26-10) complexed with digoxin and of a mutant of the Fab itself have been solved by molecular replacement. The solution strategy employed a generalization of molecular replacement. Prior to translation searches, a large number of the highest rotation-function peaks were subjected to a rigid-body refinement against the linear correlation coefficient between intensities of observed and calculated structure factors in which first the overall orientation of the model and then the orientations and translations of the individual domains (V_H, V_L, C_H1 and C_L) were refined. This procedure clearly identified the correct orientation of the search model. Furthermore, it produced a significant and unambiguous solution for the translation search. After rigid-body refinement, the *R* factor was in the low forties at 8-2·5 and 8-2·7 Å resolution for the Fab mutant and the Fab/digoxin complex, respectively. One round of simulated annealing refinement of all atomic positions reduced the *R* factor to the low twenties in both cases.

Introduction*

Molecular replacement, which is sometimes also referred to as Patterson search, involves the placement (*i.e.* rotation and translation) of the known structure of a search model in the unit cell of the target crystal in order to obtain the best agreement between calculated model diffraction data and the observed diffraction data (Hoppe, 1957; Rossmann & Blow, 1962; Huber, 1965). Unfortunately, molecular replacement often fails if the search model is too inaccurate. It does not require large structural changes to make the search model too inaccurate for molecular replacement. A case in point has been reported by Brünger, Campbell, Clore, Gronenborn, Karplus, Petsko & Teeter (1987) where molecular replacement had failed with a r.m.s. difference in backbone positions between the search model and the crystal structure of around 1·4 Å; variation of the parameters of the molecular replacement (number of reflections, resolution range, temperature factors and occupancy of atoms of the search model) made little difference.

Recently, we have generalized molecular replacement by introducing additional parameters *p* in order to make the search model more accurate (Brünger, 1990*a*). First, a conventional rotation search is carried out. The highest peaks of the rotation search are selected. Here we make the *ad hoc* assumption that the correct orientation is among the highest peaks of the rotation function. Then the rotation search is 'filtered' by employing refinements of the parameters *p* against the negative correlation coefficient PC for each selected orientation of the search model. Refinement is carried out against the negative correlation coefficient since minimization algorithms normally locate minima as opposed to maxima; a minimum of −PC corresponds to a maximum of PC

* Abbreviations: CDR, complementarity determining region; CPU, central processing unit; Fab, antigen binding fragment of an antibody; PC, standard linear correlation coefficient between $|E_{obs}|^2$ and $|E_{model}|^2$; r.m.s., root-mean-square; SA, simulated annealing; σ, standard deviation.

0108-7673/91/030195-10$03.00